

Rheology of concentrated suspension of fibers with load dependent friction coefficient

Monsurul Khan^{*1}, Rishabh V. More^{*1}, Arash Alizad Banaei², Luca Brandt³ Arezoo M. Ardekani^{1,†}

¹School of Mechanical Engineering, Purdue University, West Lafayette, IN 47907, USA

²Chemical Engineering, Stanford University, Stanford, CA 94305, USA

³Flow and SeRC (Swedish e-Science Research Centre), Department of Engineering Mechanics, KTH, SE-100 44 Stockholm, Sweden

(Received xx; revised xx; accepted xx)

We investigate the effects of fiber aspect ratio, roughness, flexibility, and volume fraction on the rheology of concentrated suspensions in a steady shear flow using direct numerical simulations. We model the fibers as inextensible continuous flexible slender bodies with the Euler-Bernoulli beam equation governing their dynamics suspended in an incompressible Newtonian fluid. The fiber dynamics and fluid flow coupling is achieved using the immersed boundary method (IBM). In addition, the fiber surface roughness might lead to inter-fiber contacts resulting in normal and tangential forces between the fibers, which follow Coulomb's law of friction. The surface roughness is modeled as hemispherical protrusions on the fiber surfaces. Their deformation results in a normal load-dependent friction coefficient. Our simulations accurately predict the experimentally observed shear thinning in fiber suspensions. Furthermore, we find that the suspension viscosity η increases with increasing the volume fraction, roughness, fiber rigidity, and aspect ratio. The increase in η is the macroscopic manifestation of a similar increase in the microscopic contact contribution to the total stress with these parameters. In addition, we observe positive and negative first N_1 and second N_2 normal stress differences, respectively, with $|N_2| < |N_1|$, in agreement with previous experiments. Lastly, we propose a modified Maron-Pierce law to quantify the reduction in the jamming volume fraction by increasing the fiber aspect ratio and roughness. Our results and analysis establish the use of fiber surface tribology to tune the suspension flow behavior.

Key words: Immersed boundary method, shear-thinning, normal stress differences, flexible fiber, rheology, fiber suspensions, dense suspensions, jamming

1. Introduction

Understanding the rheological properties of fiber suspensions is essential in many industrial applications such as paper and pulp production, biofuel production, and material reinforcement, to name a few (Bivins *et al.* 2005; Elgaddafi *et al.* 2012; Hassanpour *et al.* 2012; Lundell *et al.* 2011; Lindström & Uesaka 2008). These applications typically involve mixing, transportation, and handling concentrated fiber suspensions. Therefore, an accurate prediction of the suspension rheological properties is desirable to optimize these operations and prevent failures in industrial plants. However, fiber suspensions exhibit complex non-Newtonian behavior, such as the Weissenberg effect (Nawab & Mason 1958;

† Email address for correspondence: ardekani@purdue.edu

* Equal contributions in the writing of this manuscript

Mewis & Metzner 1974), viscoelasticity (Thalen 1964), and shear thinning (Goto *et al.* 1986; Kitano & Kataoka 1981; Bounoua *et al.* 2016*b*), which makes their flow difficult to predict and control. A better understanding of the governing physical mechanisms and the effects of various controlling parameters on suspension rheology can help alleviate these difficulties. Over the years, different parameters such as volume fraction, fiber aspect ratio, and flexibility have been identified that directly influence the suspension rheology (Wu & Aidun 2010*b*; Switzer & Klingenberg 2003; Banaei *et al.* 2020; Yamane *et al.* 1994). Typically, the fibers are assumed to be perfectly smooth (Banaei *et al.* 2020; Wu & Aidun 2010*b*). As a result, the details of inter-fiber interactions, especially surface roughness, have been ignored. However, even the so-called smoothest fibers have microscopic irregularities on their surfaces. These microscopic surface non-uniformities have been known to affect the bulk suspension rheology in dense sphere suspensions significantly (Tanner & Dai 2016; Hsu *et al.* 2018; More & Ardekani 2020*b,c,a*; Hilali *et al.* 2022). However, their role in influencing fiber suspension rheology is not completely understood.

Fiber suspensions are classified as dilute, semi-dilute, or concentrated based on the number density defined as $\frac{nL^3}{V}$, where $\frac{n}{V}$ is the number of fibers per unit volume and L is the length of each fiber. In the dilute regime, i.e., $\frac{nL^3}{V} < 1$, inter-fiber interactions are negligible. Interestingly, the stochasticity involved in the orientation changes of the fibers might result in a non-monotonic viscosity variation with volume fraction unlike in spherical particle suspensions (Blakeney 1966). In the semi-dilute regime, $1 < \frac{nL^3}{V} < \frac{L}{d}$, where d the fiber diameter, inter-fiber interactions start to influence the macroscopic properties and eventually become dominant in the concentrated regime $\frac{nL^3}{V} > \frac{L}{d}$. The viscosity of semi-dilute suspensions of rigid fibers in a Newtonian fluid is a function of the volume fraction but does not depend on the aspect ratio for sufficiently high shear rates (Bibbó 1987). The experiments by Djalili-Moghaddam & Toll (2006) found a nearly constant viscosity as a function of the shear rate in the dilute regime, whereas shear thinning was observed in the semi-dilute regime. In addition to the shear rate-dependent viscosity, fiber suspensions also exhibit non-zero normal stress differences. In a shear flow, an isolated fiber can introduce a non-zero normal stress difference, the value of which is determined by the degree of instantaneous alignment of the fiber to the flow (Batchelor 1971). Parallel plate geometries have been used to measure the normal stress differences, $N_1 - N_2$, where N_1 and N_2 are the first and second normal stress differences, respectively (Goto *et al.* 1986; Petrich *et al.* 2000; Sepehr *et al.* 2004). These studies consistently reported a positive $N_1 - N_2$, which increased with increasing particle volume fraction. Direct measurement of N_1 and N_2 observed an increase in their magnitudes when the aspect ratio decreases (Snook *et al.* 2014; Bounoua *et al.* 2016*a*).

In the semi-dilute and concentrated suspensions, the contribution of non-hydrodynamic interactions, such as frictional contacts to the suspension stress, appears (Wu & Aidun 2010*b*). Therefore, the Jeffery's model (Jeffery 1922) to calculate the stress and viscosity for dilute suspensions considering only hydrodynamic interaction does not hold in semi-dilute and concentrated regimes (Anczurowski *et al.* 1967; Okagawa & Mason 1973). Including contact interactions and the hydrodynamic interactions increases the viscosity and the first normal stress difference compared to the permissible range of Batchelor's theory (Batchelor 1971). Batchelor's theory (Batchelor 1971) considered only hydrodynamic interactions to calculate the stress in concentrated elongated particle suspensions, and hence, under-predicts the increase in viscosity and the first normal stress difference (Salahuddin *et al.* 2013). In suspensions, roughness might lead to contact and friction between the fibers, which lubrication interactions should prevent for perfectly

smooth fibers. Simulations of concentrated fiber suspensions with aspect ratio 11 – 32 showed that the inter-particle forces are responsible for the existence of first normal stress differences (Butler & Snook 2018; Snook *et al.* 2014). Moreover, increasing the inter-fiber friction coefficient between rigid fibers increases the fiber flocculation in the suspension, consequently increasing the suspension viscosity (Lindström & Uesaka 2008). However, the simplified model of a constant friction coefficient employed in these previous studies does not capture the entire physics. Experimental measurements have revealed that the friction coefficient is not constant but varies with the normal force and the roughness of the fibers (Brizmer *et al.* 2007; Huang *et al.* 2009). Hence, sophisticated models rooted in a physical understanding of the friction coefficient are needed to accurately model the inter-fiber contact dynamics. We utilize one such model in this study, as discussed in the later sections.

Fiber shape is another important factor governing suspension rheology. Slightly increasing the fiber curvature results in a change of the fiber rotation and a significant rise in the suspension viscosity compared to a straight fiber (Joung *et al.* 2001; Goto *et al.* 1986). These observations highlight the importance of fiber geometry and hence, fiber flexibility in determining the suspension rheological properties. Simulations to understand the role of flexibility by modeling fibers as a chain of rigid elements that can bend, stretch and twist observed a reduction in the period of fiber rotation with increasing flexibility (Yamamoto & Matsuoka 1993). On the bulk scale, the same model observed a decrease in the suspension viscosity with the fiber stiffness (Joung *et al.* 2001). A decrease in the relative viscosity with the ratio of the shear rate to the stiffness of the fibers was reported using a rod chain model (Switzer & Klingenberg 2003). However, this model Wu & Aidun (2010*a,b*) showed a decrease in the relative viscosity with fiber stiffness in contrast with the simulation by Switzer *et al.* Switzer & Klingenberg (2003). Thus, there is a lack of consistency and accuracy in the simulation results on the effect of fiber flexibility using the simple rod chain models. This suggests that more accurate modeling of fiber dynamics is required to capture the effects of various parameters, especially fiber flexibility. This can be achieved by modeling the fiber as a continuous object and is done in this study.

Transporting suspensions at high solid volume fractions is crucial to optimize processes and save energy in many industrial applications. However, long-lasting, dense, and system-spanning force chains can form at high solid volume fractions in frictional fiber flows, which strongly resist the flow. Jamming happens when the volume fraction is so high that the viscosity diverges and the suspension cannot flow irrespective of the applied high shear stress. Hence, it is difficult to characterize and predict the rheological properties of suspensions near jamming, which is apparent from the relatively small number of experimental studies for highly concentrated suspensions of fibers. In particular, experiments have shown that the increase in the aspect ratio of rigid fibers lowers the maximum volume fraction at which the suspension can flow (Tapia *et al.* 2017). They also observed that close to jamming volume fraction (ϕ_m), the viscosity scales as $(\phi_m - \phi)^{-1}$, where ϕ is the volume fraction of the suspension. The dependence of the jamming on the fibers' surface roughness and flexibility was mainly addressed in dry suspensions (Guo *et al.* 2015, 2020) using the discrete element method, but hasn't been studied for wet suspensions, which are the focus of this study. Although understanding the suspension rheology at high volume fractions is of great industrial importance, the effects of aspect ratio and surface roughness on the jamming transition in suspensions of flexible fibers have not been quantified yet. We quantify these effects in the present study.

The suspension microstructure is influenced by the various governing factors mentioned

above, and in turn, affects the bulk suspension rheology. Thus, understanding the relationship between these governing parameters, suspension microstructure, and macroscopic rheological properties of fiber suspensions is crucial to eliciting the underlying physical mechanisms governing the suspension rheology. Researchers have endeavored to understand the influence of some of these factors on the microstructure and rheological behavior of suspensions over the past decades, but we are still far from understanding the underlying physical mechanisms completely. To this end, we propose a numerical framework based on the immersed boundary method (IBM) (Peskin 1972) and the discrete element method (More & Ardekani 2020c) to simulate the shear flow of fiber suspensions and compute their flow properties. Our numerical model can predict the experimentally observed shear thinning behavior and quantify normal stress differences in fiber suspensions (Djalili-Moghaddam & Toll 2006). This numerical framework enables us to perform a multidimensional parametric exploration to deconvolute and explicate the effects of fiber flexibility, aspect ratio, volume fraction, and roughness on the bulk suspension rheological properties. The governing equations and the numerical model are explained in the next section, followed by results and a discussion of the effects of the governing parameters on the bulk rheological properties. Finally, we elicit the functional forms of the dependence of the jamming volume fraction on the governing parameters, which can be useful in optimizing the transport and handling of dense fiber suspensions.

2. Governing equations and numerical model

In this section, we discuss the governing equations for the suspending fluid, fiber dynamics, and inter-fiber interactions. We use the method and algorithm in Banaei *et al.* (2020), which we briefly discuss here. For detailed validation tests of the numerical method, the reader is referred to Banaei *et al.* (2020).

2.1. Flow field equations

We consider an incompressible Newtonian suspending fluid, the flow of which is governed by the Navier-Stokes equations. In an inertial Cartesian frame of reference, the dimensionless momentum and mass conservation equations for an incompressible fluid are:

$$\frac{\partial \mathbf{u}}{\partial t} + \nabla \cdot (\mathbf{u} \otimes \mathbf{u}) = -\nabla p + \frac{1}{Re} \nabla^2 \mathbf{u} + \mathbf{f}, \quad (2.1)$$

$$\nabla \cdot \mathbf{u} = 0, \quad (2.2)$$

where \mathbf{u} is the velocity field, p the pressure, and \mathbf{f} the volume force to account for the suspending fibers; $Re = \rho \dot{\gamma} L^2 / \eta$ is the Reynolds number where ρ and η are the fluid density and dynamic viscosity, L is the characteristic length scale which is also the fiber length, and $\dot{\gamma}$ is the applied shear rate. Details on the fluid-structure interaction force \mathbf{f} are given in Sec. 2.3.

2.2. Fiber dynamics

We model the fiber as a continuous flexible slender body. The dynamics of a thin flexible fiber are described by the Euler-Bernoulli Beam equations under the constraint of inextensibility (Segel & Handelman 2007). The equation of motion for each fiber in dimensionless form is:

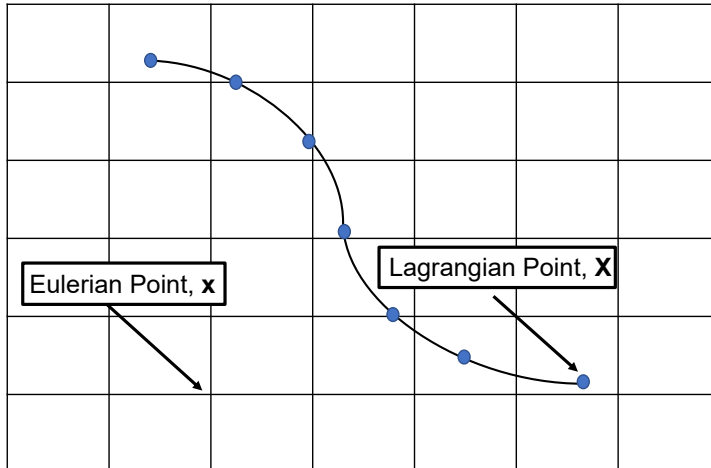


Figure 1: Schematic of the Eulerian and the Lagrangian grids. The black dots denote the Lagrangian points through which the position of the fibers are defined.

$$\left(\frac{\rho_f}{\rho A_f}\right) \frac{\partial^2 \mathbf{X}}{\partial t^2} = \frac{\partial^2 \mathbf{X}_{fluid}}{\partial t^2} + \frac{\partial}{\partial s} \left(T \frac{\partial \mathbf{X}}{\partial s} \right) - \frac{\partial^2}{\partial s^2} \left(B \frac{\partial^2 \mathbf{X}}{\partial s^2} \right) + \frac{\Delta \rho}{\rho A_f} Fr \frac{\mathbf{g}}{g} - \mathbf{F} + \mathbf{F}^f \quad (2.3)$$

where s is the curvi-linear coordinate along the fiber, $\mathbf{X} = (x(s, t), y(s, t), z(s, t))$ is the position of the Lagrangian points on the fiber axis, T the tension force along the fiber axis, $Fr = g/(L\dot{\gamma}^2)$ the Froude number with \mathbf{g} the gravitational acceleration vector and $g = |\mathbf{g}|$, $B = \frac{EI}{\rho_f \dot{\gamma}^2 L^4}$ the dimensionless bending rigidity with E the elastic modulus and I the second moment of inertia for fiber cross-section, \mathbf{F} the fluid-solid interaction force, \mathbf{F}^f the net interaction force on the fiber due to neighboring fibers, ρ_f the fiber linear density (mass per unit length), and A_f the fiber cross sectional area. Equation 2.3 is made dimensionless by the following characteristic scales: L for length, $U_\infty = \dot{\gamma}L$ for velocity, L/U_∞ for time, $\rho_f U_\infty^2$ for tension, $\rho_f U_\infty^2 L^2$ for bending and $\rho_f U_\infty^2 / L$ for force. $\Delta \rho = \rho_f - \rho A_f$ denotes the linear density difference between the fibers and the surrounding fluid, with $\Delta \rho = 0$ for the neutrally buoyant case. Finally, the inextensibility condition is expressed as

$$\frac{\partial \mathbf{X}}{\partial s} \cdot \frac{\partial \mathbf{X}}{\partial s} = 1. \quad (2.4)$$

2.3. Numerical method

The fluid-solid coupling is achieved using the Immersed Boundary Method (IBM) (Peskin 1972). In the IBM, the geometry of the object is represented by a volume force distribution \mathbf{f} that mimics the effect of the object on the fluid. In this method, two sets of grid points are needed: a fixed Eulerian grid \mathbf{x} for the fluid and a moving Lagrangian grid \mathbf{X} for the flowing deformable structure as shown in figure 1. Each fiber has its own Lagrangian coordinate system. In this study we assume the fibers to be neutrally buoyant, so equation (2.3) is modified as:

$$\frac{\partial^2 \mathbf{X}}{\partial t^2} = \frac{\partial^2 \mathbf{X}_{fluid}}{\partial t^2} + \frac{\partial}{\partial s} \left(T \frac{\partial \mathbf{X}}{\partial s} \right) - B \frac{\partial^4 \mathbf{X}}{\partial s^4} - \mathbf{F} + \mathbf{F}^f, \quad (2.5)$$

where the LHS term is the acceleration of the fiber, and the RHS consists of the acceleration of the fluid particle at the fiber location and the different forces acting on the

fibers. This is done to avoid the singularity of the coefficient matrix in the fiber equation of motion (equation 2.3) for the neutrally buoyant case, as reported by Pinelli *et al.* (2017). To solve for the fiber position in equation 2.5, we first solve the Poisson's equation for tension (Huang *et al.* 2007) obtained by combining equations 2.4 and 2.5, which is given as:

$$\frac{\partial \mathbf{X}}{\partial s} \cdot \frac{\partial^2}{\partial s^2} \left(T \frac{\partial \mathbf{X}}{\partial s} \right) = \frac{1}{2} \frac{\partial^2}{\partial t^2} \left(\frac{\partial \mathbf{X}}{\partial s} \cdot \frac{\partial \mathbf{X}}{\partial s} \right) - \frac{\partial^2 \mathbf{X}}{\partial t \partial s} \cdot \frac{\partial^2 \mathbf{X}}{\partial t \partial s} - \frac{\partial \mathbf{X}}{\partial s} \cdot \frac{\partial}{\partial s} (\mathbf{F}^a + \mathbf{F}^b + \mathbf{F}^f - \mathbf{F}) \quad (2.6)$$

where $\mathbf{F}^a = \frac{\partial^2 \mathbf{X}_{\text{fluid}}}{\partial t^2}$ is the acceleration of the fluid particle at the fiber location and $\mathbf{F}^b = -B \frac{\partial^4 \mathbf{X}}{\partial s^4}$ is the bending force. As the fibers are freely suspended in the fluid medium, we impose zero force, torque and tension at the free ends. So,

$$\frac{\partial^2 \mathbf{X}}{\partial s^2} = 0, \quad \frac{\partial^3 \mathbf{X}}{\partial s^3} = 0, \quad \text{and} \quad T = 0. \quad (2.7)$$

At each time step, the fluid velocity is first interpolated onto the Lagrangian grid points using the smooth Dirac delta function, δ (Roma *et al.* 1999):

$$\mathbf{U}_{ib} = \int_V \mathbf{u}(\mathbf{x}, t) \delta(\mathbf{X} - \mathbf{x}) dV, \quad (2.8)$$

The fluid and solid equations are then coupled by the fluid-solid interaction force,

$$\mathbf{F} = \frac{\mathbf{U} - \mathbf{U}_{ib}}{\Delta t}, \quad (2.9)$$

where \mathbf{U}_{ib} is the interpolated fluid velocity at the Lagrangian points defining the fibers, \mathbf{U} is the velocity of the Lagrangian points and Δt is the time step. The Lagrangian force is then extrapolated onto the fluid grid as

$$\mathbf{f}(\mathbf{x}, t) = \frac{\pi}{4} r_p^2 \int_L \mathbf{F}(\mathbf{x}, t) \delta(\mathbf{X} - \mathbf{x}) ds. \quad (2.10)$$

Here $r_p = d/L$, is the slenderness ratio of the fiber, which is the inverse of its aspect ratio defined as $AR = L/d$. The interaction force can be further split into $\mathbf{F}^f = \mathbf{F}^{lc} + \mathbf{F}^c$, where \mathbf{F}^{lc} and \mathbf{F}^c are the lubrication correction, and contact interaction, respectively, as explained below.

2.4. Lubrication interactions

To accurately resolve the lubrication interactions between the fibers when the inter-fiber gap falls below a few grid-sizes, we use the lubrication correction model of Lindström & Uesaka (2008). The lubrication force model is based on the solution for two infinitely long cylinders adapted to two different configurations: parallel cylinders or at an arbitrary angle. The first-order approximation of the lubrication force for the non-parallel case was derived by Yamane *et al.* (1994) and is given as follow:

$$\mathbf{F}_1^l = \frac{-12}{\text{Re} \sin \alpha} \frac{\dot{\mathbf{h}}}{h}, \quad (2.11)$$

where h is the shortest distance between the cylinders, $\dot{\mathbf{h}}$ is the relative normal velocity between the closest points on the fibers, and α is the contact angle. The first order approximation of the lubrication force per unit length between parallel cylinders was

derived by Kromkamp *et al.* (2005):

$$\begin{aligned} \mathbf{F}_2^l &= \frac{-4}{\pi \text{Re} r_p^2} (A_1 + A_2 \frac{h}{a}) \left(\frac{h}{a}\right)^{-3/2} \dot{\mathbf{h}}, \\ A_1 &= 3\pi\sqrt{2}/8, A_2 = 207\pi\sqrt{2}/160, \end{aligned} \quad (2.12)$$

here a is the cylinder radius ($a = d/2$). Based on equations 2.11 and 2.12, the following approximation of the lubrication force for two finite cylinders is (Lindström & Uesaka 2008):

$$\mathbf{F}^l = \min(\mathbf{F}_1^l/\Delta s, \mathbf{F}_2^l). \quad (2.13)$$

The force for the non-parallel case is divided by the Lagrangian grid spacing Δs to calculate the force per unit length. The numerical method implemented to calculate the lubrication force is discussed in Banaei *et al.* (2020), and hence is not repeated here. As the distance between the fibers becomes of the order of the mesh size, hydrodynamic interactions are not well resolved; to address this issue, we introduce a lubrication correction force (Lindström & Uesaka 2008). When the shortest distance between two Lagrangian points becomes lower than $d/4$, we introduce lubrication correction as: $\mathbf{F}^{lc} = \mathbf{F}^l - \mathbf{F}_0^l$, where F_0^l is the lubrication force at a $d/4$ distance.

The lubrication forces diverge as the minimum inter-fiber separation decreases, and theoretically should prevent the fibers from coming into direct contacts. However, the thin lubrication film between close fibers can break because of the presence of irregularities on their surfaces leading to a direct contact between the fibers and hence, contact forces. Direct contacts also give rise to non-negligible friction between the fibers. The following section provides an overview of the implemented contact model.

2.5. Contact model

With increasing volume fraction, the surrounding fibers hinder the free rotation of nearby fibers, giving rise to fiber-fiber contacts that influences the micro-structure. Hence, the importance of accurately modelling the contact dynamics cannot be over-stressed, as routinely done when studying dry fiber suspensions (Guo *et al.* 2015) and more recently spherical particle suspensions (Gallier *et al.* 2014; More & Ardekani 2020*c*). In recent years, researchers have investigated the effects of inter-particle contacts on the rheology of suspensions by using experimentally validated models, which have been proven to be effective in quantitatively reproducing many experimental findings (Mari *et al.* 2014; More & Ardekani 2020*c,b*). Specifically, the single-asperity model of the surface roughness has been widely used owing to its simplicity and effectiveness (Gallier *et al.* 2014; Lobry *et al.* 2019; More & Ardekani 2020*a,b,c*). Hence, we take the same approach and model the asperity as a hemispherical bump on the fiber surface as shown in figure 2a. Actual asperities might not be just hemispherical and can come in a variety of geometries (Tanner & Dai 2016). However, on average we can model their behavior by approximately assuming them hemispherical as routinely done in the tribology literature (Broedersz & MacKintosh 2014).

Let us consider two fibers as shown in figure 2a with diameter d and length L having surface roughness height h_r . The contact between the fibers occurs when the smallest inter-fiber separation distance h becomes smaller than h_r . As a result, the asperity deforms which results in forces normal, \mathbf{F}_n , and tangential, \mathbf{F}_t to the fiber surface. The normal contact force is given by the Hertz law:

$$\mathbf{F}_n = -F_0 \left(\frac{|\delta|}{L}\right)^{3/2} \mathbf{n}, \quad (2.14)$$

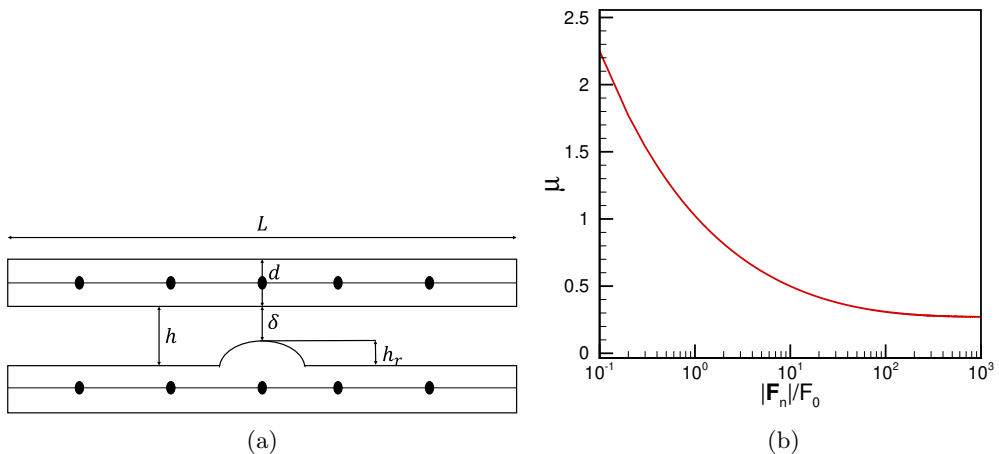


Figure 2: (a) A sketch of the roughness model, L and d are the length and diameter of the fiber, respectively, h_r is the roughness height, and $\delta = h - h_r$ is the surface overlap. Contact occurs when $\delta \leq 0$. Dots along the axes of the fibers indicate Lagrangian points. (b) Friction coefficient μ as a function of the dimensionless contact normal force (equation 2.16).

where δ is the surface overlap defined as $\delta = h - h_r$, and $F_0/L^{3/2}$ is the normal stiffness, which is a function of the fiber material properties, and the roughness size (Lobry *et al.* 2019; More & Ardekani 2020c). We use F_0 as the characteristic contact force scale in this study. The contact happens when $\delta \leq 0$. The Coulomb's friction law gives the tangential force:

$$\mathbf{F}_t = \mu |\mathbf{F}_n| \frac{\mathbf{F}_t}{|\mathbf{F}_t|}, \quad (2.15)$$

where μ is the friction coefficient. Several studies have assumed a constant friction coefficient when numerically studying the dynamics of fiber suspensions (Banaei *et al.* 2020; Stickel *et al.* 2009). In reality, the coefficient of friction depends on many factors such as the fiber material and the roughness size, which are implicitly included in the normal force via the normal stiffness $F_0/L^{3/2}$ (Lobry *et al.* 2019; More & Ardekani 2020c). Hence, a normal load dependent coefficient of friction is a more accurate physical description than a simple constant. We use the Brizmer model (Brizmer *et al.* 2007) for μ , which was derived from the measurements between a hemisphere and a flat surface and validated using the finite element analysis (Brizmer *et al.* 2007), which makes it applicable to a wide range of materials and conditions (Brizmer *et al.* 2007; Lobry *et al.* 2019; More & Ardekani 2020c). It is given by:

$$\mu = 0.27 \coth \left[0.27 \left(\frac{|\mathbf{F}_n^{(i,j)}|}{F_0} \right)^{0.35} \right], \quad (2.16)$$

where F_0 is the characteristic contact force scale introduced in equation 2.14. Equation 2.16 is a decreasing function of $|\mathbf{F}_n^{(i,j)}|/F_0$ as illustrated in figure 2b. Thus, the coefficient of friction decreases with increasing the normal force between the contacting fibers (which is equivalent to increasing asperity deformation in equation 2.14) and attains a plateau at high normal loads. Moreover, to avoid overlap of the fibers with the walls,

we implement a repulsive force having the form of a Morse potential as:

$$\emptyset = D_e [e^{-2\beta(r_f - r_e)} - 2e^{-\beta(r_f - r_e)}], \quad (2.17)$$

where D_e is the interaction strength, β a geometric scaling factor, r_f the distance between a point on a fiber and the wall, and r_e the zero-cut-off force distance. The repulsive between the elements i and j is the derivative of the potential function,

$$F_r = -\frac{d\emptyset}{dr} d_{ij}, \quad (2.18)$$

where d_{ij} is the unit vector in the direction joining the contact point.

After calculating the short range interactions between fibers, the tension inside each fiber is computed by solving equation 2.6. Then, the new fiber position is obtained by solving equation 2.5 and the fluid equations are advanced in time. The fluid equations are solved with a second-order finite difference method on a fix staggered grid. The equations are advanced in time by a semi-implicit fractional step-method, where the second order Adams-Bashforth method is used for the convective terms, a Helmholtz equation is built with the diffusive and temporal terms, and all other terms are treated explicitly (Alizad Banaei *et al.* 2017).

2.6. Boundary conditions and Domain size

We investigate suspensions of flexible fibers in a Couette flow, by varying the volume fraction (ϕ), aspect ratio ($AR = L/d$), flexibility ($1/\tilde{B}$), and roughness (ϵ_r). The fibers are suspended in a channel with upper and lower walls moving in the x -direction with opposite velocities of magnitude $U_\infty = \dot{\gamma}L$. No-slip and no-penetration boundary conditions are imposed on the wall and periodicity is assumed in the stream-wise (x), and span-wise (z) directions. The fibers are initially distributed randomly. For this study, we consider a domain of size $5L \times 8L \times 5L$ and $80 \times 128 \times 80$ grid points in the stream-wise (x), wall normal (y) and span-wise direction (z), respectively. The coordinate system and the simulation setup is illustrated in figure 3. Simulations with bigger domain, higher grid and time resolution, e.g., 1.5, 2, 2.5 and 3 times the current domain, grid and time resolution show a negligible (less than 2 %) change in the averaged steady state suspension viscosity. Finally, 17 Lagrangian points over the fiber length are enough to resolve the case with the highest fiber flexibility. The required time-step to capture the fiber dynamics is $\Delta t = 10^{-4}$. The suspension is simulated until a statistically steady viscosity is observed and the mean values presented are obtained discarding the initial transients.

2.7. Stress and bulk rheology calculations

The bulk stress in the suspension quantifies the rheological properties of the suspension. The total stress, Σ_{ij} , can be written as

$$\Sigma_{ij} = \Sigma_{ij}^0 + \Sigma_{ij}^f, \quad (2.19)$$

$$\begin{aligned} \Sigma_{ij}^0 &= \frac{Re}{V} \int_{V-\Sigma V_f} (-p\delta_{ij} + \frac{2}{Re}e_{ij})dV, \\ \Sigma_{ij}^f &= \frac{Re}{V} \sum \int_{V_f} \sigma_{ij}dV - \frac{Re}{V} \int_V u'_i u'_j dV. \end{aligned} \quad (2.20)$$

Here Σ_{ij}^0 is the viscous fluid stress and results in a dimensionless contribution of 1 (or $\eta\dot{\gamma}$ in the dimensional form) in a simple shear flow after subtracting the isotropic fluid

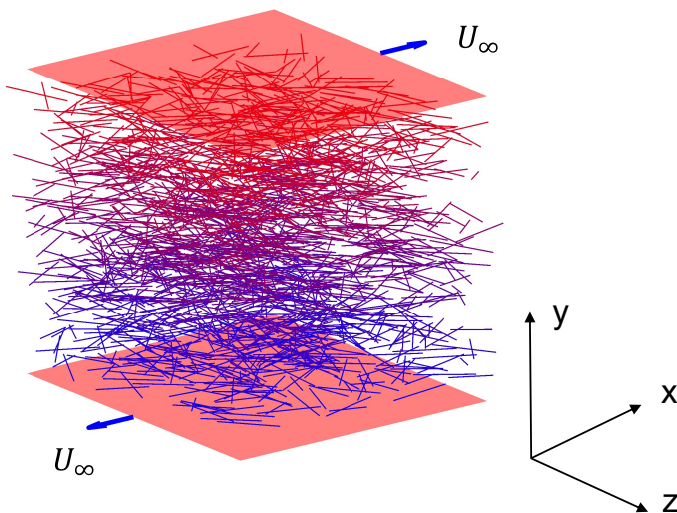


Figure 3: Simulation setup of the shear flow of a fiber suspension. The top and bottom walls move with velocities $U_\infty = \dot{\gamma}L$ in the directions shown by the arrows.

pressure. Σ_{ij}^f is the stress generated by the presence of fibers and inter-fiber interactions. Moreover, V is the total volume, V_f the volume occupied by each fiber, $e_{ij} = \frac{\partial u_i}{\partial x_j} + \frac{\partial u_j}{\partial x_i}$ represents the strain rate tensor, \mathbf{u}' the velocity fluctuations, and σ_{ij} is the fiber stress. The fiber stress σ_{ij} can be decomposed into two parts:

$$\int_{V_f} \sigma_{ij} dV = \int_{A_f} \sigma_{ik} x_j n_k dA - \int_{V_f} \frac{\partial \sigma_{ik}}{\partial x_k} x_j dV, \quad (2.21)$$

where A_f represents the surface area of each fiber and \mathbf{n} is the unit surface normal vector on the fiber pointing outwards. The first term is called the stresslet, and the second term indicates the acceleration stress (Guazzelli & Morris 2011). The second term is identically zero for neutrally buoyant fibers when the relative acceleration of the fiber and fluid is zero. Because $\sigma_{ik} n_k$ is simply the force per unit area acting on the fibers (Batchelor 1971), it can be written for slender bodies as:

$$\int_{A_f} \sigma_{ik} x_j n_k dA = -r_p^2 \int_L F_i x_j ds, \quad (2.22)$$

where F_i is the fluid solid interaction force as defined in equation 2.9. The term r_p^2 arises from choosing the linear density instead of the volume density in the characteristic force scale. Finally, the total fiber stress is defined as:

$$\Sigma_{ij}^f = -\frac{Re r_p^2}{V} \sum_1^n \int_L F_i x_j ds - \frac{Re}{V} \int_V u'_i u'_j dV. \quad (2.23)$$

From the results of our simulations, we observe that, the last term related to the velocity fluctuations is very small compared to the stresslet and can be neglected for the range of Reynolds number considered here. The calculated bulk stress tensor can now be used to quantify the rheological properties of the suspensions. The relative viscosity η_r is defined as:

$$\eta_r = \frac{\eta_{eff}}{\eta}, \quad (2.24)$$

where η_{eff} is the effective suspension viscosity. The relative viscosity in terms of the bulk shear stress is:

$$\eta_r = 1 + \Sigma_{xy}^f, \quad (2.25)$$

with Σ_{xy}^f being the ensemble averaged shear stress arising from the presence of the fibers, fluid-fiber, and inter-fiber interactions. The first (N_1) and second (N_2) normal stress differences are defined as:

$$N_1 = \Sigma_{xx} - \Sigma_{yy}, \quad (2.26a)$$

$$N_2 = \Sigma_{yy} - \Sigma_{zz} \quad (2.26b)$$

There are two main contributions to the bulk stress: 1) the hydrodynamic contribution Σ_{ij}^h , and 2) the contact contribution Σ_{ij}^c . These will be useful in the following sections for analysing the simulation results. The contact contribution can be calculated from the ensemble average of the contact stresslet given by:

$$\Sigma_{ij}^c = -\frac{Re r_p^2}{V} \sum_1^n \int_L F_i^c x_j ds. \quad (2.27)$$

Thus, the hydrodynamic contribution can be simply obtained as $\Sigma_{ij}^h = \Sigma_{ij}^0 + (\Sigma_{ij}^f - \Sigma_{ij}^c)$. This splitting of the total stress allows us to track the variations in the contributions from different mechanisms to the observed rheological behavior of the suspension with varying parameters, e.g., $\eta_r^h = \Sigma_{xy}^h$, and $\eta_r^c = \Sigma_{xy}^c$ are the hydrodynamic and the contact contributions to the relative viscosity η_r , respectively.

2.8. Simulation parameters

The aim of this study is to investigate the effects of dimensionless shear rate ($\dot{\Gamma}$), fiber volume fraction (ϕ), flexibility ($1/\bar{B}$), aspect ratio (AR), and roughness (ϵ_r) of the fibers on the suspension rheology in the presence of friction. First, we define the dimensionless numbers reported in this study.

The relative importance of contact to the hydrodynamic forces can be estimated using dimensionless shear rate, $\dot{\Gamma}$ defined as

$$\dot{\Gamma} = \frac{6\pi\eta d^2 \dot{\gamma}}{F_0}, \quad (2.28)$$

where $\dot{\gamma}$ is the imposed shear rate, and η is the viscosity of the suspending fluid. To keep the Reynolds number $Re = \rho\dot{\gamma}L^2/\eta$ constant, we vary $\dot{\Gamma}$ by varying the characteristic contact force scale F_0 . It is well known that the rate-dependent rheology of suspensions is determined by the competition between various stress (force) scales (Guazzelli & Pouliquen 2018; More & Ardekani 2020d). Hence, by changing the value of F_0 , we vary the relative contribution from the contact and hydrodynamic forces in the suspension. Typically, F_0 depends on the fiber material properties like Young's modulus, elastic modulus, Poisson's ratio, etc. (Brizmer *et al.* 2007). In some cases, this results in a very high value of F_0 restricting the time-step size to impractically small values ($< 10^{-7}$)

Table 1: Range of parameters explored in this study

ϵ_r	$\dot{\Gamma}$	ϕ	AR	\tilde{B}
0.005 – 0.10	1 – 1000	0.05 – 0.46	10 – 16	0.005 – 0.2

making the simulations computationally expensive. Hence, to resolve these numerical issues and gain some fundamental understanding, we vary F_0 in orders of magnitudes of the hydrodynamic stress scale, i.e., $6\pi\eta d^2\dot{\gamma}$, as routinely done for spherical suspensions (Gallier *et al.* 2014; Mari *et al.* 2014; More & Ardekani 2020*b*). This automatically allows us to vary $\dot{\Gamma}$, without changing the Reynolds number. The dimensionless roughness height ϵ_r is defined as

$$\epsilon_r = \frac{h_r}{d} \quad (2.29)$$

where h_r is the surface roughness height. The fiber bending rigidity \tilde{B} , which quantifies the fiber flexibility is made dimensionless by the viscous stress scale as:

$$\tilde{B} = \frac{EI}{\eta\dot{\gamma}L^4} \quad (2.30)$$

In the literature, the fiber rigidity is quantified using the dimensionless bending rigidity (\tilde{B}) (Switzer & Klingenberg 2003; Keshtkar *et al.* 2009; Bounoua *et al.* 2016*b*), and/or bending ratio (BR) Wu & Aidun (2010*b*); Snook *et al.* (2014). From their respective definitions, one can see that they can be used interchangeably. The Bending ratio, BR ($BR = \frac{\tilde{B}(\ln 2r_e - 1.5) * 32}{\pi}$) is just a multiple of the dimensionless bending rigidity, \tilde{B} . So, in this study, effects of varying the dimensionless bending rigidity are equivalent to that observed by varying the bending ratio. This dimensionless bending rigidity \tilde{B} is related to the bending rigidity B reported in equation (2.3) by

$$\tilde{B} = \frac{\pi}{4} r_p^2 Re B. \quad (2.31)$$

The volume fraction of the suspension is defined as

$$\phi = \frac{n\pi r_p^2}{4V}. \quad (2.32)$$

In summary, the functional form of the stress can be written as :

$$\begin{aligned} \frac{\Sigma_{xy}}{\eta\dot{\gamma}} &= \eta_r \left(\frac{n\pi r_p^2}{4V}, \frac{L}{d}, \frac{h_r}{d}, \frac{EI}{\eta\dot{\gamma}L^4}, \frac{6\pi\eta d^2\dot{\gamma}}{F_0} \right) \\ &= \eta_r(\phi, AR, \epsilon_r, \tilde{B}, \dot{\Gamma}) \end{aligned} \quad (2.33)$$

We simulate a shear flow by varying the fiber bending rigidity in the range $0.005 \leq \tilde{B} \leq 0.2$, the dimensionless roughness height in the range $0.005 \leq \epsilon_r \leq 0.10$, the dimensionless shear rate in the range $1 \leq \dot{\Gamma} \leq 1000$, and the aspect ratio in the range $10 \leq AR \leq 16$. Note that the lower (higher) \tilde{B} value corresponds to flexible (rigid) fibers. The range of parameters explored in the present work are summarized in table 1.

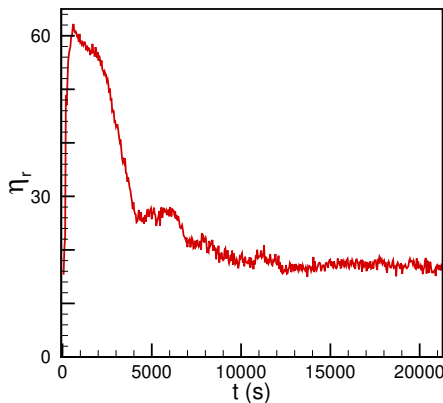


Figure 4: Transient viscosity from the initial state to the steady state flow. The roughness height is fixed to $\epsilon_r = 0.05$, bending rigidity to $\tilde{B} = 0.07$, aspect ratio to $AR = 16$, and volume fraction to $\phi = 15\%$.

3. Results and discussion

This section presents the results of the numerical simulations. Sections 3.1-3.4 focus on the shear rate dependent behavior and explain the effects of varying the fiber volume fraction, aspect ratio, flexibility, and roughness. Section 3.5 presents the effects of the governing parameters on the normal stress differences N_1 and N_2 .

We make all the quantities dimensionless using the scaling mentioned in section 2. The suspension is simulated until a statistically steady viscosity is observed and the mean values presented are obtained discarding the initial transients as shown in figure 4. The structural solver has been validated by comparing four distinct cases in a previous study Alizad Banaei *et al.* (2017) and hence, not repeated here for brevity.

3.1. Shear-thinning and increase of η_r with the volume fraction

We start with analyzing the computed relative viscosity, η_r as a function of the dimensionless shear rate, $\dot{\Gamma}$, for different volume fractions, as shown in figure 5a. We observe that the viscosity reduces with increasing the shear rate, indicating a shear thinning behavior. Eventually, it plateaus at high shear rates. To quantify the degree of shear thinning, we use the following power law curve fit to the simulation data.

$$\eta_r(\dot{\Gamma}) = k\dot{\Gamma}^{-m}. \quad (3.1)$$

Here k is the flow consistency index and $m > 1$ is the shear thinning index, which quantifies the strength of the shear thinning effect. As shown in figure 5a, with increasing the volume fraction of the suspension, the magnitudes of k and n increase, indicating a rise in the shear thinning effect with increasing the volume fraction.

Increase in the shear stress directly increases the magnitude of the normal force between the fibers, which in turn results in the reduction of the friction coefficient according to equation 2.16. Hence, with all other parameters maintained constant, we expect a drop in the coefficient of friction with increasing shear rate (which is directly proportional to the shear stress), leading to a decrease in the relative viscosity, similar to the findings of More *et al.* More & Ardekani (2020b). This becomes clear when we look at the average coefficient of friction (μ_{avg}) as depicted in figure 5b. μ_{avg} is the time average of the

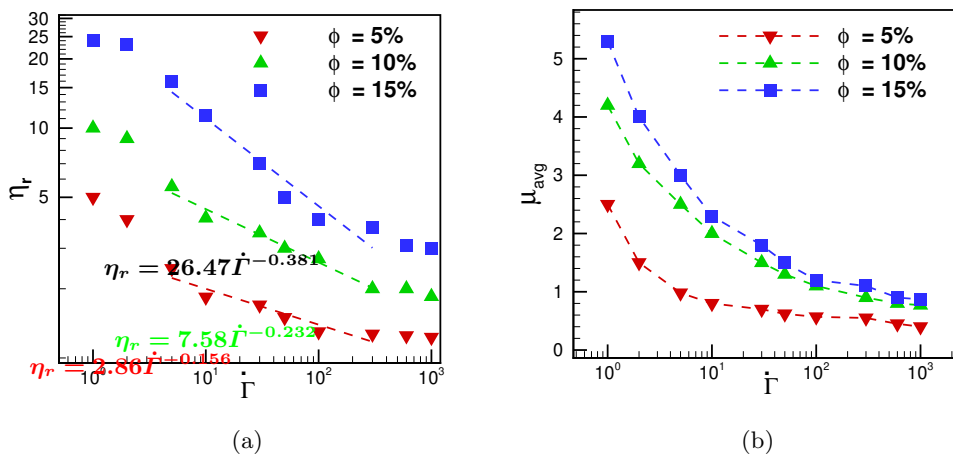


Figure 5: (a) Relative viscosity η_r of fiber suspensions versus the dimensionless shear rate $\dot{\Gamma}$ at different volume fractions. The dashed line represents the power law fit as described in equation 3.1. The power law indices for different volume fractions are - $\phi = 5\%$: $k = 2.86$, $m = 0.156$; $\phi = 10\%$: $k = 7.58$, $m = 0.232$; and $\phi = 15\%$: $k = 26.47$, $m = 0.381$. (b) Variation in the average coefficient of friction μ_{avg} for the suspensions with dimensionless shear rate for different volume fractions. The roughness height is fixed to $\epsilon_r = 0.05$, bending rigidity to $\tilde{B} = 0.07$ and aspect ratio to $AR = 16$ for all cases. The model implemented in this study can reproduce the experimentally observed shear thinning behavior in suspensions of fibers.

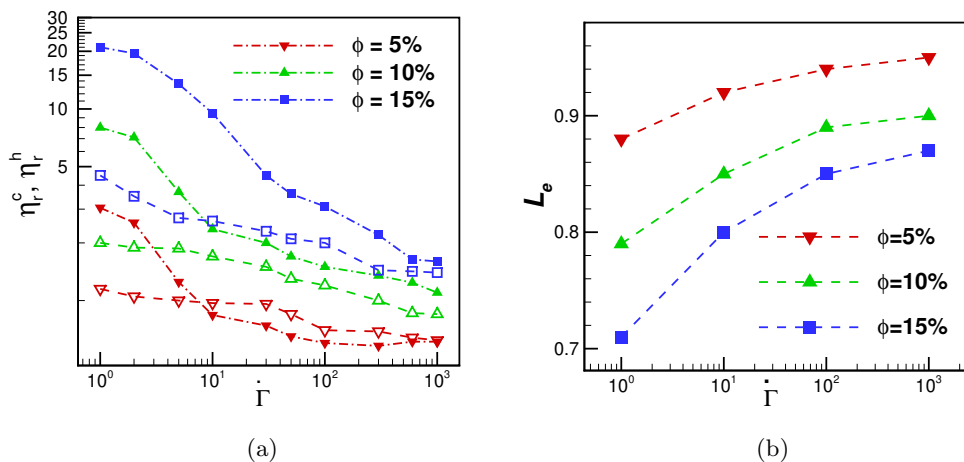


Figure 6: (a) Hydrodynamic η_r^h and contact η_r^c contributions to the relative viscosity for three different volume fractions as in figure 5a. Open symbols: hydrodynamic contribution. Closed symbols: contact contribution. The sum of the hydrodynamic and contact contribution is the total relative viscosity as reported in figure 5a. (b) Ensemble averaged end-to-end distance L_e of the suspended fibers as a function of dimensionless shear rate for different volume fractions. The roughness height is fixed to $\epsilon_r = 0.05$, bending rigidity to $\tilde{B} = 0.07$ and aspect ratio to $AR = 16$ for all cases.

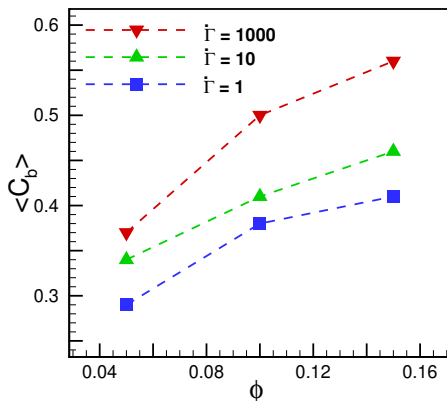


Figure 7: The mean orbit constant $\langle C_b \rangle$ for different volume fraction. As the volume fraction increase, fibers align more strongly in the flow gradient plane.

coefficient of friction, μ , between all the contacting pairs in the suspension when the simulations reach statistically steady state. This reduction in μ_{avg} with $\dot{\Gamma}$ results in a decrease in the dominant contact contribution η_r^c to the bulk suspension viscosity as depicted in figure 6a. On the other hand, a constant friction coefficient results in a constant shear rate independent viscosity as showed in our previous publication Khan *et al.* (2022). Moreover, the hydrodynamic contribution η_r^h to the relative viscosity also decreases with $\dot{\Gamma}$ adding to the shear thinning. We can explain the reduction of the hydrodynamic contribution with shear rate by calculating the fiber deformation as reported in figure 6b. As the shear rate increases, fibers' deformation decreases and they align more with the flow direction, eventually decreasing the hydrodynamic contributions. Moreover, the orbit constant, C_b , when averaged over the fibers in the suspension, is the measure of the orientation distribution. The ratio $C/(C+1)$ is used to define C_b where,

$$C = \frac{1}{A} \tan \theta_z (A^2 \cos^2 \theta_y + \sin^2 \theta_y)^{1/2} \quad (3.2)$$

where θ_z is the angle of the fiber with respect to the span-wise direction (z -axis), and angle θ_y is the angle between the gradient direction (y -axis) and the projection of the fiber on the flow-gradient (x - y) plane. The average orbit constant $\langle C_b \rangle$ goes to 1 if all fibres are aligned in the flow-gradient plane and equals zero if the fibres are aligned with the span-wise direction (z -axis). Figure 7 shows that as the volume fraction increases, fibers align more strongly to the flow gradient plane, similar to the findings of previous simulations Wu & Aidun (2010b); Lindström & Uesaka (2008); Snook *et al.* (2014). Moreover, as the shear rate increases, fibers also tend to align with the flow-gradient direction.

It is well known that the viscosity of suspensions increases with increasing the particle phase volume fraction and it diverges at a certain maximum volume fraction beyond which the suspension does not flow, the so-called the jamming fraction ϕ_m . We observe the same behavior for fiber suspensions in our simulations. With all other parameters held fixed, the suspension viscosity increases with increasing the volume fraction as depicted in figure 8a. The reason behind this increase is the increase in the fiber contribution to the total stress with increase in their numbers per unit volume. In our simulations, we quantify this contribution using Σ_{xy}^f as discussed in sec. 2.7. The fiber contribution to the total stress increases with the volume fraction due to the increase in the average

number of contacting fibers ($\langle n_c \rangle$) as also depicted in figure 8a. $\langle n_c \rangle$ is the time average of the average number of fibers that come into contact with another fiber once the simulations reach statistically steady state. The consequence of the increase in $\langle n_c \rangle$ with ϕ is the rise in the contribution of the hydrodynamic as well as contact interactions to the total viscosity as shown in figure 8b. While the hydrodynamic contribution increase weakly, the contact contribution becomes significant and dominant at volume fraction greater than 5% because of the substantial rise in $\langle n_c \rangle$. This observation underlines the impact of contacts in the rheology of fiber suspensions in the semi-dilute and the concentrated regime.

The variation in η_r with ϕ can be captured by the the well known Maron-Pierce law (Maron & Pierce 1956), which has been extensively used in the literature to model the behavior of smooth spherical particle suspensions. However, to capture the behavior of rough suspensions, a modified Maron-Pierce law is needed (More & Ardekani 2020c). The following modified Maron-Pierce law (Maron & Pierce 1956; More & Ardekani 2020c) is used to fit the data in the figure 8a:

$$n_r = \alpha(1 - \phi/\phi_m)^{-\beta}, \quad (3.3)$$

with the coefficient α , the exponent β , and the jamming fraction ϕ_m depending on the aspect ratio and roughness of the fibers. As depicted by the solid lines in figure 8a, equation 3.3 does a good job in modelling the viscosity as a function of volume fraction. We find that the relative viscosity diverges near the jamming transition with a scaling of $(\phi_m - \phi)^{-1}$ in contrast with $(\phi_m - \phi)^{-2}$, the behavior observed for a suspension of spheres (More & Ardekani 2020a,b,c). The scaling obtained here for flexible fibers is $(\phi_m - \phi)^{-1}$, whereas for rigid fibers the scaling was found as $(\phi_m - \phi)^{-0.90}$ Tapia *et al.* (2017). In the next subsection, we turn our attention to the effect of the fiber aspect ratio on suspension rheology.

3.2. Increase in aspect ratio of the fibers reduces the suspension flowability

As shown in figure 8a, the average number of contact for a fiber increase with increasing volume fraction. The same is true with increasing the fiber aspect ratio, AR (Williams & Philipse 2003). In a concentrated suspension, elongated fibers have a larger probability of inter-fiber contacts. As a result, there is an increase in the contact force which leads to a caging effect. Thus, the viscosity increases with the aspect ratio for a fixed volume fraction as shown in figure 9a. As a result, the viscosity diverges at a critical volume fraction ϕ_m that depends on the aspect ratio as shown in figure 9a. The solid lines demonstrate the best fit with equation (3.3). The values for α and ϕ_m obtained after fitting are presented in table 2. From the data, we observe a reduction of ϕ_m from ≈ 0.47 to ≈ 0.22 with increasing the fiber AR from 10 to 16 for suspensions with $\epsilon_r = 0.05$, and $\tilde{B} = 0.07$. Figure 9b shows the data after rescaling the volume fraction by ϕ_m , which leads to a collapse of the data indicating that it is the distance of ϕ from the jamming fraction ϕ_m that determines the suspension rheology. Hence, ϕ/ϕ_m can be used as a design parameter for tuning the fiber suspension rheology, as it is easier to measure and control compared to other parameters like size distribution, roughness and friction in real-world suspensions. In the next subsection, we focus on the effect of roughness of the fibers on the suspension rheology.

3.3. Roughness increases suspension viscosity

In figure 10, we present snapshots of a thin slice in the middle of the simulation cell for suspension of fibers with roughness $\epsilon_r = 0.005$ and $\epsilon_r = 0.05$. We observe that at high

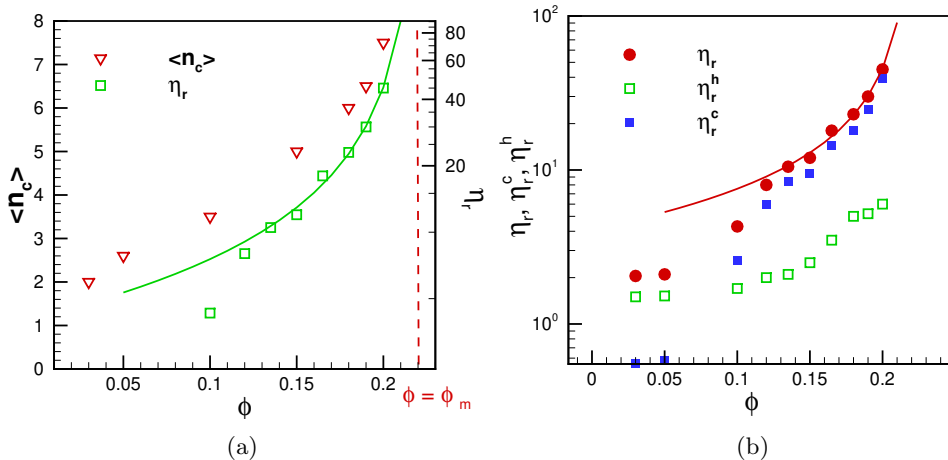


Figure 8: (a) The average number of contacting fibers and viscosity variation vs. volume fraction. (b) Hydrodynamic and contact contributions to the relative viscosity as a function of volume fraction. The average number of contacting fibers increases with the volume fraction which in turn increases the relative contribution from the contact interactions to the total viscosity. The green solid line in (a) represents the fitting with a modified Maron-Pierce law (Maron & Pierce 1956) described as $n_r = \alpha(1 - \phi/\phi_m)^{-\beta}$, with parameters $\alpha = 4.42$, $\phi_m = 0.22$ and $\beta = 1$. The dashed red line shows the jamming volume ($\phi_m = 0.22$) for the current case where roughness height was fixed to $\epsilon_r = 0.05$, shear rate to $\dot{\Gamma} = 10$, bending rigidity to $\tilde{B} = 0.07$, and aspect ratio to $AR = 16$.

Table 2: Fitting parameters for different aspect ratios for a fixed roughness height, $\epsilon_r = 0.05$, bending rigidity, $\tilde{B} = 0.07$ and dimensionless shear rate, $\dot{\Gamma} = 10.0$. $\beta = 1$ for all cases.

AR	α	ϕ_m
10	1.54	0.47
12	2.58	0.42
14	3.24	0.32
16	4.42	0.22

surface roughness fibers tend to agglomerate more compared to smooth fibers, increasing the overall flow resistance of the suspension. We quantify the effect of roughness by showing the increase in relative viscosity with roughness for a suspension with 15% volume fraction at three different shear rates. The increase of viscosity with roughness is higher at low shear rates than at high shear rates. This is directly linked to the steep variation of μ at low normal loads and it attaining a plateau at high normal loads (eq. 2.16 and figure 2b). The stress, which directly determines the normal force between the contacting fibers, is low at low shear rate values. Hence, even a small change in the roughness size results in a large change in the friction at low shear rates as depicted by the variation of the average value of the friction coefficient, μ_{avg} , displayed in figure 11b. On the contrary, at high shear rate values, μ does not change much with increasing the

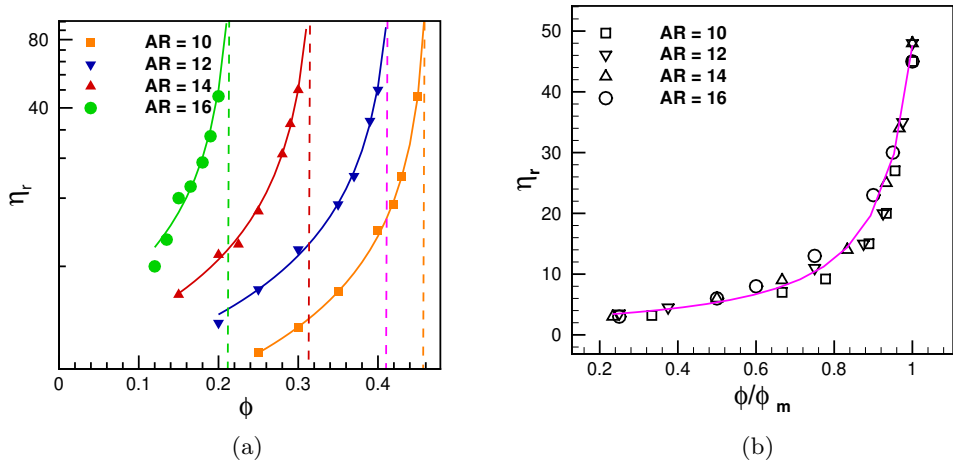


Figure 9: (a) Relative viscosity η_r vs. volume fraction ϕ for different aspect ratios AR . Solid lines are the fitting curve using equation 3.3. The vertical dashed line shows the jamming volume fraction for different aspect ratios. (b) Re-scaled rheological data for different aspect ratios. All simulations were performed for a fixed roughness $\epsilon_r = 0.05$ and bending rigidity, $\tilde{B} = 0.07$. The jamming fraction reduces with aspect ratio for a given shear rate. Re-scaling the volume fraction by ϕ_m leads to a collapse of the viscosity curves, indicating that the aspect ratio determines the maximum volume fraction once the fiber flexibility and roughness are fixed.

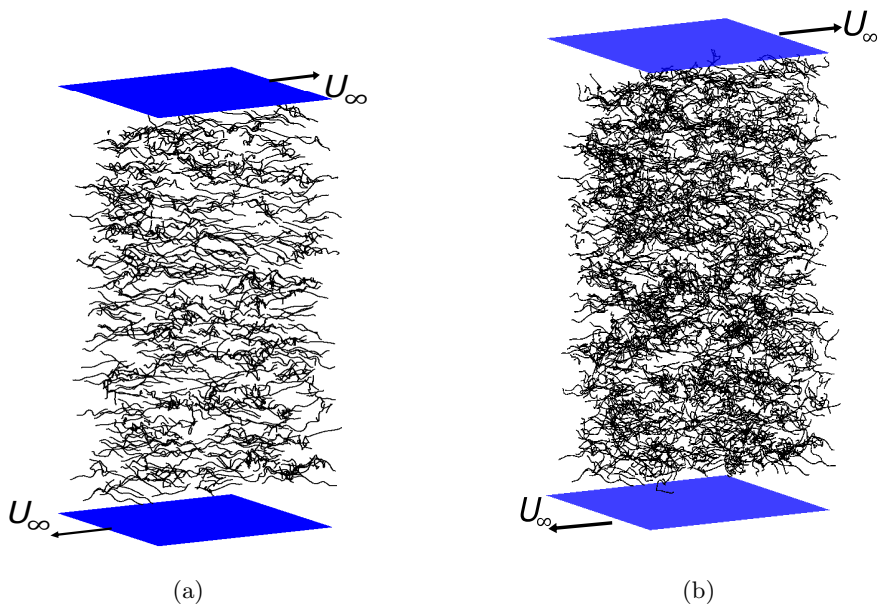


Figure 10: Simulation snapshots at a thin slice in the middle of the simulation cell after shearing to a shear rate of $\dot{\Gamma} = 10$ with bending rigidity, $\tilde{B} = 0.07$, aspect ratio, $AR = 16$, and roughness height, (a) $\epsilon_r = 0.005$, (b) $\epsilon_r = 0.05$. Rough fibers tend to agglomerate more compared to smooth fibers.

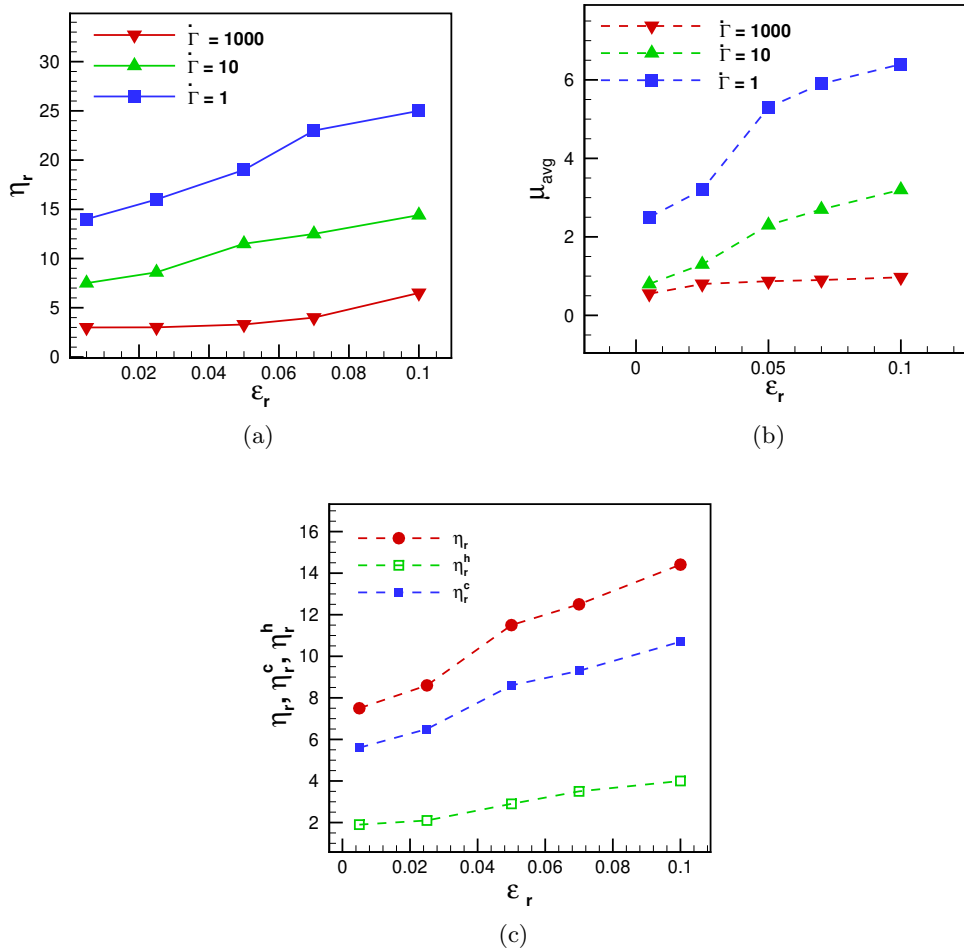


Figure 11: (a) The relative viscosity of fiber suspension vs. the roughness height, and (b) variation in the average coefficient of friction between fibers in the suspensions with roughness at three different shear rates. For these simulations volume fraction is fixed to $\phi = 15\%$, aspect ratio to $AR = 16$, and bending rigidity to $\tilde{B} = 0.07$. The relative viscosity increases with the increase in the surface roughness of the fibers as a consequence of increase in the μ_{avg} . (c) Contribution to the total relative viscosity from contact and hydrodynamic interactions at a fixed shear rate, $\dot{\Gamma} = 10$.

roughness as it attains a plateau (equation 2.16). The increase in the friction as shown by the increase in μ_{avg} with roughness in figure 11b is the reason behind the increase in the suspension viscosity with fiber roughness. The consequences of the rise in the average inter-fiber friction with roughness can be understood by analyzing the different contributions to the total relative viscosity in the suspension as shown in figure 11c. Here, we report the contribution of contact and hydrodynamic interactions to the total viscosity at different values of roughness ϵ_r for a fixed shear rate, $\dot{\Gamma} = 10$. As the fiber roughness increases, the contribution of contact forces to the total viscosity increases significantly, while the hydrodynamic contribution increases weakly. We display the smooth and rough

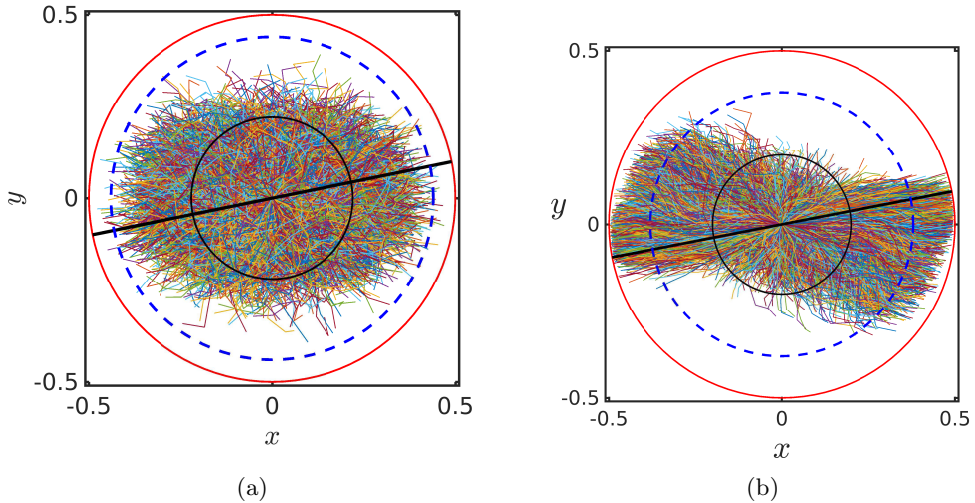


Figure 12: Co-located filaments projected on the shear plane for roughness (a) $\epsilon_r = 0.005$, and (b) $\epsilon_r = 0.05$. The solid red line represents the circles with diameter equal to the fiber length, the blue dashed line is the circle with diameter equal to the mean end to end distance and the black circles have diameter equal to the minimum end to end distance between fibers. The solid black line shows the average orientation of the fibers with respect to the wall. All simulations were performed with dimensionless shear rate $\dot{\Gamma} = 10$, volume fraction $\phi = 15\%$, aspect ratio $AR = 16$, and bending rigidity $\tilde{B} = 0.07$.

fibers co-located with centers at the origin in in figure 12. Increasing the roughness height ($\epsilon_r = 0.05$) causes larger deformation of the fibers compared to the smooth fibers ($\epsilon_r = 0.005$); increasing the hydrodynamic contribution. Moreover we note that the fibers' alignment with the flow direction does not change much with roughness.

As increasing the fiber roughness leads to an increase in the suspension viscosity, we expect the jamming fraction to reduce with increasing the fiber roughness. The effects of varying the roughness size ϵ_r from 0.01 to 0.10 for a fixed aspect ratio $AR = 12$ is shown in figure 13a. Again, the modified Maron-Pierce law (equation 3.3) is used to quantify the effects of roughness on the jamming fraction ϕ_m and the coefficient α . The fitting parameters are presented in table 3, whereas the solid lines in figure 13a represent the fitting curve given by equation (3.3). We find that the relative viscosity diverges near the jamming transition with a scaling of $(\phi_m - \phi)^{-1}$, similarly to the cases with different aspect ratios discussed above. These results confirm that the jamming fraction decreases with increasing the roughness size. For the smoothest case, $\epsilon_r = 0.01$, we find $\phi_m = 0.48$, whereas for the roughest case, $\epsilon_r = 0.1$, ϕ_m is as low as 0.41. The decrease in ϕ_m is due to an increase in the effective volume with the roughness height that results in a denser contact network (More & Ardekani 2020*c,b*). It eventually leads to an increase in the viscosity and a decrease in the jamming volume fraction as shown in figure 13b. From these findings, we can conclude that to increase the flowability of concentrated fiber suspensions, we need to break down longer fibers into smaller ones and make their surfaces smoother.

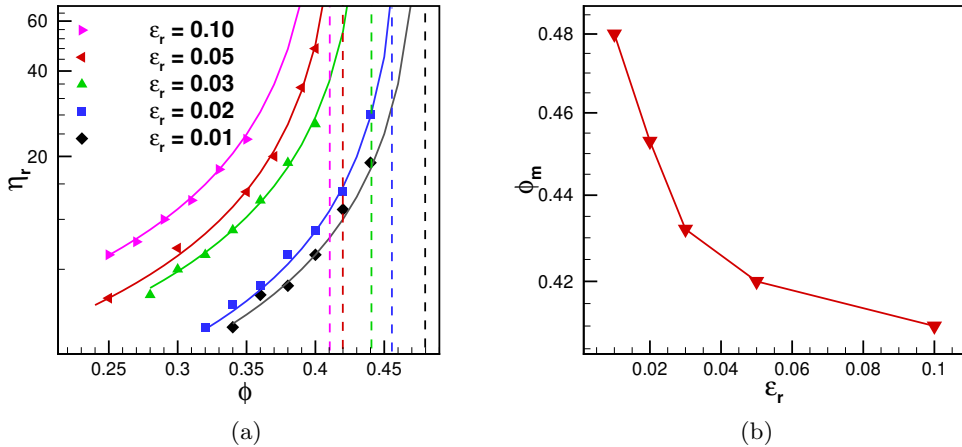


Figure 13: (a) Relative viscosity vs volume fraction for different surface roughness values. Solid lines are the fitting curves using equation 3.3. The vertical dashed line shows the jamming volume fraction for different roughness heights. (b) The jamming volume fraction vs. roughness height. All simulations were performed for a fixed bending rigidity, $\tilde{B} = 0.07$, aspect ratio, $AR = 12$ and dimensionless shear rate, $\dot{\Gamma} = 10.0$.

Table 3: Fitting parameters for different roughness values for a fixed aspect ratio, $AR = 12$, bending rigidity, $\tilde{B} = 0.07$ and dimensionless shear rate, $\dot{\Gamma} = 10.0$. $\beta = 1$ for all cases.

ϵ_r	α	ϕ_m
0.01	1.51	0.48
0.02	2.10	0.45
0.03	2.50	0.43
0.05	2.58	0.42
0.10	3.50	0.41

3.4. Effects of fiber flexibility

Flexible fibers, like deformable spheres, align with the flow direction more easily than stiff fibers as shown in figure 14, thus, causing lower resistance to their flow compared to rigid fibers. As a result, flexible fiber suspensions have lower viscosity compared to rigid fiber suspensions as demonstrated in figure 15a; in agreement with experiments (Goto *et al.* 1986; Sepehr *et al.* 2004; Switzer & Klingenberg 2003). However, simulations with fibers modelled as chains of beads had predicted a rise in the suspension viscosity with an increase in the fiber flexibility (Wu & Aidun 2010b), which is inconsistent with experiments (Goto *et al.* 1986; Sepehr *et al.* 2004). The bending and twisting of the individual beads at their joints cause additional stresses than for continuous fibers that can only bend, and hence, result in the observed rise in suspension viscosity with flexibility. The splitting of the total relative viscosity in the hydrodynamic and the contact contributions reveals the impact of fiber flexibility on the fiber dynamics as depicted in

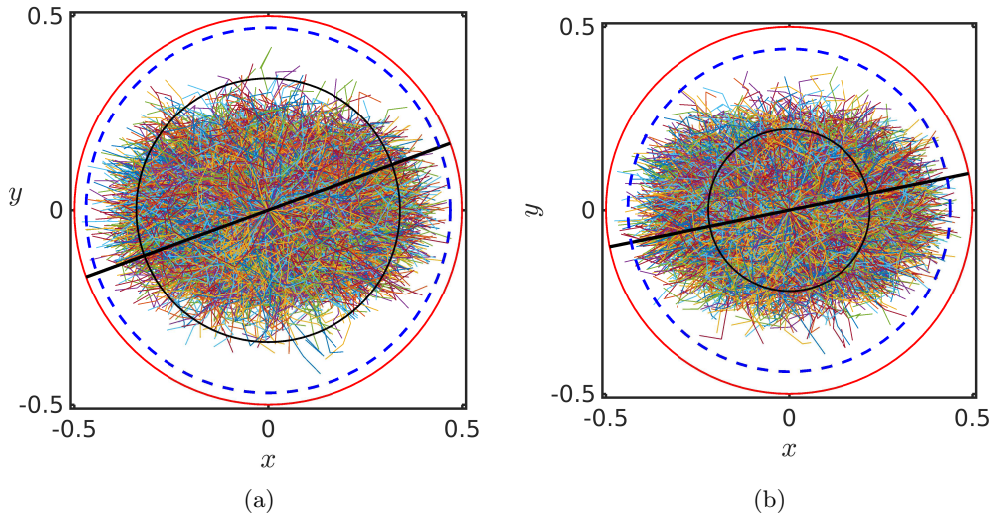


Figure 14: Co-located filaments projected on the shear plane for bending rigidity (a) $\tilde{B} = 0.10$, (b) $\tilde{B} = 0.07$. The solid red line represents the circles with diameter equal to the fiber length, the blue dashed line is the circle with diameter equal to the mean end to end distance and the black circles have diameter equal to the minimum end to end distance between fibers. The solid black line shows the average orientation of the fibers with respect to the wall. All simulations were performed with dimensionless shear rate $\dot{\Gamma} = 10$, roughness $\epsilon_r = 0.005$, volume fraction $\phi = 15\%$, and aspect ratio $AR = 16$. Increasing flexibility aligns the fibers with the flow.

figure 15b. An increase in the fiber flexibility (\tilde{B} decreases) increases the hydrodynamic contribution. As a result, flexible fibers (lower \tilde{B}) tend to be curved instead of maintaining a straight shape as shown in figure 15c, where we present time and ensemble averaged end-to-end distance L_e of the suspended fibers as a function of their bending rigidity for different shear rates. A curved fiber has a larger tumbling frequency than a straight fiber, and therefore, develops larger hydrodynamic stresses (Tozzi *et al.* 2008). It is also clear that the contact contribution, which dominates the hydrodynamic contribution, increases with the fiber rigidity and is the main responsible for the higher relative viscosity at higher bending rigidity.

3.5. Normal stress differences

In fiber suspensions, normal stress differences inevitably arise due to the presence of hydrodynamics and inter-particle interactions (Keshtkar *et al.* 2009). We present the effect of fiber flexibility on the first (N_1) and second (N_2) normal stress difference in figure 16. The first normal stress difference N_1 is positive as shown in figure 16a, in agreement with previous studies (Snook *et al.* 2014; Keshtkar *et al.* 2009). We notice that as the fiber rigidity increases, the first normal stress difference starts to decrease, in agreement with experiment reported by Keshtkar *et al.* (2009). As the fiber rigidity increases further, we observe that there is a weak minimum for the lowest shear rate, which is also in agreement with previous reported theoretical (Batchelor 1971) and computational studies (Wu & Aidun 2010b). Furthermore, the location of minimum N_1 shifts towards larger \tilde{B} as the shear rate is increased. Moreover, we note that to find

[1t]

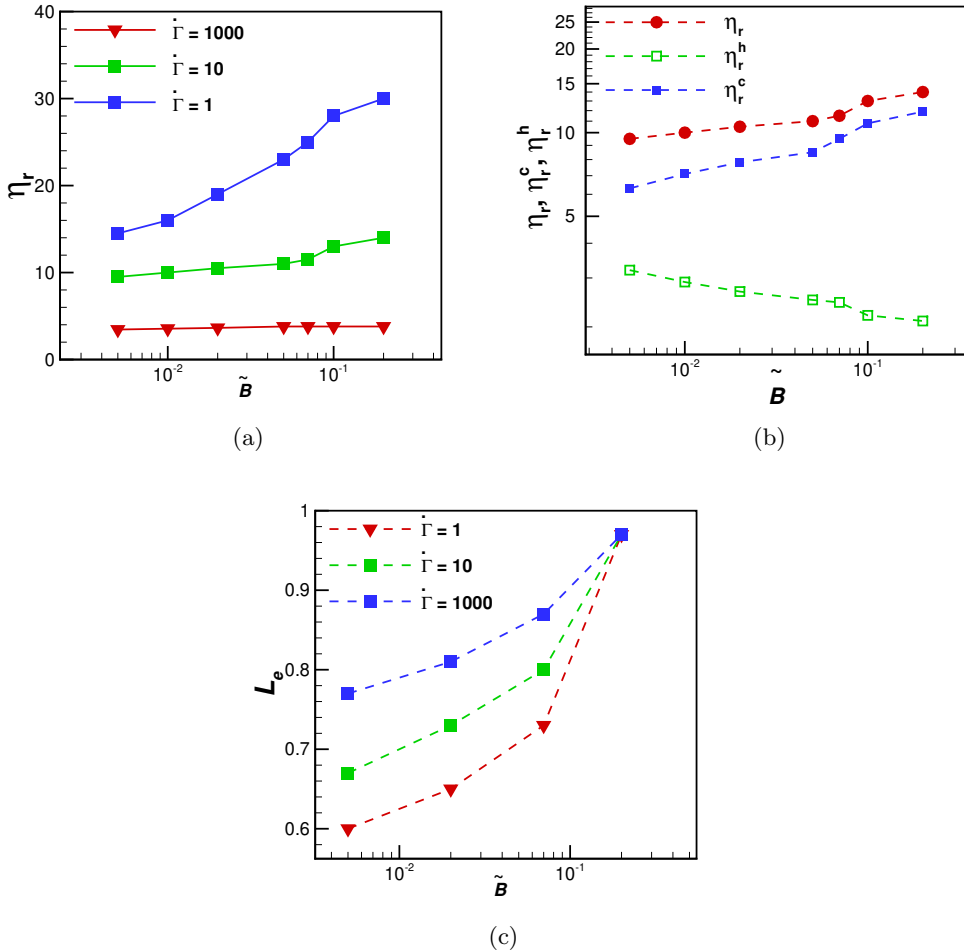


Figure 15: (a) Relative viscosity vs. bending rigidity at three different shear rates, (b) the contributions to the total relative viscosity from contact and hydrodynamic interactions for $\dot{\Gamma} = 10$, and (c) ensemble averaged end-to-end distance L_e of the suspended fibers as a function of their bending rigidity for different shear rates. All the cases consider have volume fraction $\phi = 15\%$, roughness $\epsilon_r = 0.05$, and aspect ratio $AR = 16$. Increase in the viscosity with the bending rigidity is consistent with experiments (Goto *et al.* 1986; Sepehr *et al.* 2004).

critical bending ratio at different shear rate, we need to explore very stiff fibers like Wu & Aidun (2010b), however that is out of scope for our current study due to time step constrain. On the other hand, the second normal stress N_2 is negative as shown in figure 16b. Moreover, the magnitudes of N_2 decrease as the fibers become more rigid, with a more (less) pronounced decrease at lower (high) shear rates. Several studies with rigid fibers observed a much smaller second normal stress compared to the first normal stress which can therefore be neglected in different applications. (Petrich *et al.* 2000; Sepehr *et al.* 2004). On the contrary, experimental and numerical study of rigid fibers by Snook *et al.* (2014) indicated non-negligible second normal stress, which is approximately

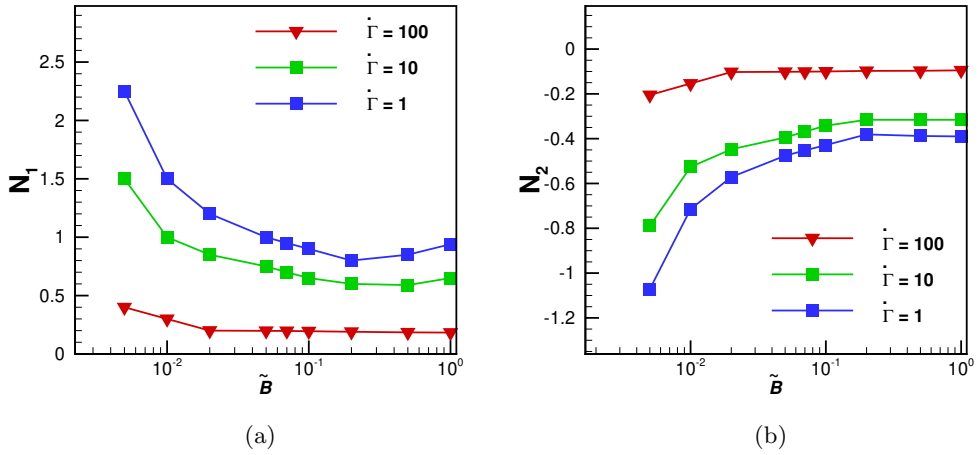


Figure 16: a) The dimensionless first, and b) second normal stress as a function bending rigidity for different shear rates. Here volume fraction $\phi = 15\%$, roughness $\epsilon_r = 0.05$, and aspect ratio $AR = 16$ are fixed. The first normal stress difference is positive and decreases as the fibers become more rigid; in agreement with the observation of Keshtkar *et al.* (2009). The second normal stress is negative with a decreasing magnitude with increasing fiber rigidity.

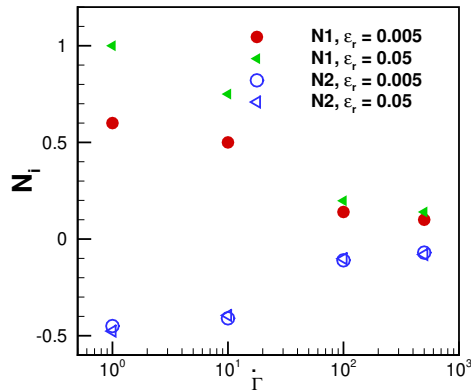


Figure 17: Variation of N_1 and N_2 with shear rate for $\phi = 15\%$ with a constant bending rigidity, $\tilde{B} = 0.05$ (\circ for $\epsilon_r = 0.005$ and \triangleleft for $\epsilon_r = 0.05$). Filled symbols are for N_1 and hollow symbol are for N_2 . All simulations were performed with volume fraction $\phi = 15\%$ and aspect ratio $AR = 16$. This graph indicates that the surface roughness increases N_1 while the N_2 stays nearly constant.

half of the first normal stress difference. We observe that the magnitude of N_2 is smaller than that of N_1 , reported in figure 16. Finally, figure 17 presents the variation of N_1 and N_2 with the shear rate $\dot{\Gamma}$ for 15% volume fraction for smooth ($\epsilon_r = 0.005$) and rough ($\epsilon_r = 0.05$) fiber suspensions. We notice that N_1 increases with the roughness height,

whereas N_2 does not change noticeably, similarly to the case of suspensions of rough spheres (More & Ardekani 2020c).

4. Conclusion

We performed numerical simulations to investigate the rheological behavior of concentrated fiber suspensions for a range of volume fraction ϕ , aspect ratios AR , bending rigidity \tilde{B} , and roughness ϵ_r . We modelled fibers as one-dimensional in-extensible slender bodies suspended in an incompressible Newtonian fluid. The fiber dynamics is resolved using the Euler-Bernoulli beam equation, while the immersed boundary method is utilized to resolve the fluid-fiber interactions. In addition, we modelled the fiber roughness as a hemispherical asperity on the fiber surface. As the fibers come into contact, the asperity deforms giving rise to normal and tangential contact forces and consequently friction. We used Coulomb's law of friction with a friction coefficient μ decreasing with the normal contact force as a more accurate description than a constant coefficient of friction. Such a load-dependent friction coefficient has been measured experimentally and confirmed using a finite-element analysis (Brizmer *et al.* 2007). The numerical model presented here can quantitatively capture the experimentally observed shear thinning in fiber suspensions (Bounoua *et al.* 2016b) as well as the variations in normal stress differences with different governing parameters.

Our results show that the suspension relative viscosity η_r increases with increasing volume fraction ϕ , roughness ϵ_r , and bending rigidity \tilde{B} . As volume fraction increases, the average number of contacting fibers $\langle n_c \rangle$ increases and hence, the relative contribution from contact interactions to the bulk stress increases. This causes the observed rise in the relative viscosity. The increase in relative viscosity with roughness is mainly attributed to the increase of the contact-force contribution to the total stress due to the rise in the average coefficient of friction, μ_{avg} . This also results in an increase in the normal stress differences N_1 and N_2 . Because of the steep variation of the friction coefficient with the normal load (see the experimentally validated friction model in equation 2.16) at low normal loads (hence, low stress in the suspension), a greater increment in relative viscosity η_r with roughness ϵ_r , volume fraction ϕ , and bending rigidity \tilde{B} at lower shear rates is observed. On the other hand, the friction coefficient μ attains a plateau at high normal loads (hence, high stress), which also results in a flattening of the relative viscosity η_r with roughness, volume fraction, and bending rigidity at higher shear rates.

We have presented the macroscopic flow properties of the suspensions and discussed the stress budget as well as fiber deformation for varying the fiber rigidity and roughness. Our results show that more rigid fibers resist deformation and do not align with the flow. As a result, they create less ordered structures which increase the resistance to the shear flow, consequently increasing the suspension viscosity. Moreover, we find that fibers deform more when their surface roughness increases, an effect similar to that observed when increasing the fiber flexibility; however, rough fibers do not align with the flow as flexible fibers. As a result, the relative viscosity increases with increasing roughness, but it decreases when increasing the fiber flexibility. So, even though the mesoscopic effect (fiber deformation and alignment) of these microscopic parameters (flexibility and roughness) is the same, they results in a different macroscopic flow behavior. Furthermore, our results for the normal stress differences showed that the first normal stress difference is positive and the second normal stress difference is negative, which is consistent with previous studies (Keshtkar *et al.* 2009; Snook *et al.* 2014). Flexible fiber suspensions have a larger magnitude of the first and second normal stress differences, also in agreement with available experiments. Keshtkar *et al.* (2009).

We also explored the divergence of the relative viscosity as the suspension volume fraction approaches the maximum flowable limit, i.e, the jamming fraction ϕ_m . We presented a modified Maron-Pierce law to quantify the effects of the governing parameters on ϕ_m . In particular, we show that increasing AR and ϵ_r decrease ϕ_m . Re-scaling ϕ by ϕ_m collapses the η_r data for varying AR on a single curve denoting that changing the fiber aspect ratio principally affects the maximum volume fraction if the roughness is fixed. The decrease in the jamming volume fraction with aspect ratio is attributed to the increase in the number of contacts and the contact forces, which in turn increases the stress in the suspension at the same shear rate. We also quantified the jamming fraction for different roughness heights. As the roughness height increases, the suspension jams at a lower volume fraction. With an increase in the roughness height, the effective volume fraction increases, resulting in a denser contact network. As a result the average coefficient of friction increases, which in turn reduces the jamming volume fraction. We found the viscosity to diverge as $(\phi_m - \phi)^{-1}$, in contrast with spherical suspensions, where viscosity diverges as $(\phi_m - \phi)^{-2}$.

Our results demonstrate the importance of accurately modelling the inter-fiber interactions to capture the experimentally observed shear rate-dependent rheological behavior of fiber suspensions. We showed that the fiber tribology governs the suspension flow behavior. Since it is challenging to modify the coefficient of friction, we can modify the fiber surface properties that influence the friction (e.g., roughness) to tune the suspension flow properties. Additionally, we found that to have higher solid concentrations, desired in industrial applications, we should breakdown the fibers into smaller ones, pre-treat them to be more flexible, and to make the surface smoother. Finally, the mono-asperity contact model implemented here could be refined by taking into account a finite number of asperities, possibly growing with the load. In addition, it will be an interesting study to find how the model to predict anisotropic diffusivity changes from previous study Salahuddin *et al.* (2012) when the effect of friction is considered for numerical simulations of dense fiber suspension. More generally, due to the complexity of the friction forces at the microscopic scale and the number of parameters that are potentially relevant in the surface physical chemistry, the next step would be to quantitatively determine the frictional law from colloidal probe AFM measurements.

ACKNOWLEDGEMENT

AMA would like to acknowledge financial support from the Department of Energy via grants EE0008256 and EE0008910. This work used the Extreme Science and Engineering Discovery Environment (XSEDE) (Towns *et al.* 2014), which is supported by the National Science Foundation grant number ACI-1548562 through allocations TG-CTSI190041. L.B. acknowledges financial support from the Swedish Research Council (VR) and the INTERFACE research environment (Grant No. VR 2016-06119).

REFERENCES

- ALIZAD BANAEI, A. , LOISEAU, J.-C. , LASHGARI, I. & BRANDT, L. 2017 Numerical simulations of elastic capsules with nucleus in shear flow. *European Journal of Computational Mechanics* **26** (1-2), 131–153.
- ANCZUROWSKI, E. , COX, R. & MASON, S. 1967 The kinetics of flowing dispersions: Iv. transient orientations of cylinders. *Journal of Colloid and Interface Science* **23** (4), 547–562.
- BANAEI, A. A. , ROSTI, M. E. & BRANDT, L. 2020 Numerical study of filament suspensions at finite inertia. *Journal of Fluid Mechanics* **882**.
- BATCHELOR, G. 1971 The stress generated in a non-dilute suspension of elongated particles by pure straining motion. *Journal of Fluid Mechanics* **46** (4), 813–829.

- BIBBÓ, M. A. 1987 Rheology of semiconcentrated fiber suspensions. PhD thesis, Massachusetts Institute of Technology.
- BIVINS, C. H. , BONEY, C. , FREDD, C. , LASSEK, J. , SULLIVAN, P. , ENGELS, J. , FIELDER, E. O. , GORHAM, T. , JUDD, T. , MOGOLLON, A. E. S. & OTHERS 2005 New fibers for hydraulic fracturing. *Oilfield Review* **17** (2), 34–43.
- BLAKENEY, W. R. 1966 The viscosity of suspensions of straight, rigid rods. *Journal of Colloid and Interface Science* **22** (4), 324–330.
- BOUNOUA, S. , KUZHIR, P. & LEMAIRE, E. 2016a Normal stress differences in non-brownian fiber suspensions. *Journal of rheology* **60** (4), 661–671.
- BOUNOUA, S. , LEMAIRE, E. , FÉREC, J. , AUSIAS, G. & KUZHIR, P. 2016b Shear-thinning in concentrated rigid fiber suspensions: Aggregation induced by adhesive interactions. *Journal of Rheology* **60** (6), 1279–1300.
- BRIZMER, V. , KLIGERMAN, Y. & ETSION, I. 2007 Elastic–plastic spherical contact under combined normal and tangential loading in full stick. *Tribology Letters* **25** (1), 61–70.
- BROEDERSZ, C. P. & MACKINTOSH, F. C. 2014 Modeling semiflexible polymer networks. *Reviews of Modern Physics* **86** (3), 995.
- BUTLER, J. E. & SNOOK, B. 2018 Microstructural dynamics and rheology of suspensions of rigid fibers. *Annual Review of Fluid Mechanics* **50**, 299–318.
- DJALILI-MOGHADDAM, M. & TOLL, S. 2006 Fibre suspension rheology: effect of concentration, aspect ratio and fibre size. *Rheologica acta* **45** (3), 315–320.
- ELGADDAFI, R. , AHMED, R. , GEORGE, M. & GROWCOCK, F. 2012 Settling behavior of spherical particles in fiber-containing drilling fluids. *Journal of Petroleum Science and Engineering* **84**, 20–28.
- GALLIER, S. , LEMAIRE, E. , PETERS, F. & LOBRY, L. 2014 Rheology of sheared suspensions of rough frictional particles. *Journal of Fluid Mechanics* **757**, 514–549.
- GOTO, S. , NAGAZONO, H. & KATO, H. 1986 The flow behavior of fiber suspensions in newtonian fluids and polymer solutions. *Rheologica acta* **25** (2), 119–129.
- GUAZZELLI, E. & MORRIS, J. F. 2011 *A physical introduction to suspension dynamics*, , vol. 45. Cambridge University Press.
- GUAZZELLI, É. & POULIQUEN, O. 2018 Rheology of dense granular suspensions. *Journal of Fluid Mechanics* **852**.
- GUO, Y. , LI, Y. , LIU, Q. , JIN, H. , XU, D. , WASSGREN, C. & CURTIS, J. S. 2020 An investigation on triaxial compression of flexible fiber packings. *AIChE Journal* **66** (6), e16946.
- GUO, Y. , WASSGREN, C. , HANCOCK, B. , KETTERHAGEN, W. & CURTIS, J. 2015 Computational study of granular shear flows of dry flexible fibres using the discrete element method. *Journal of Fluid Mechanics* **775**, 24–52.
- HASSANPOUR, M. , SHAFIGH, P. & MAHMUD, H. B. 2012 Lightweight aggregate concrete fiber reinforcement—a review. *Construction and Building Materials* **37**, 452–461.
- HILALI, M. M. , PAL, S. , MORE, R. V. , SAIVE, R. & ARDEKANI, A. M. 2022 Sheared thick-film electrode materials containing silver powders with nanoscale surface asperities improve solar cell performance. *Advanced Energy and Sustainability Research* **3** (1), 2100145.
- HSU, C.-P. , RAMAKRISHNA, S. N. , ZANINI, M. , SPENCER, N. D. & ISA, L. 2018 Roughness-dependent tribology effects on discontinuous shear thickening. *Proceedings of the National Academy of Sciences* **115** (20), 5117–5122.
- HUANG, F. , LI, K. & KULACHENKO, A. 2009 Measurement of interfiber friction force for pulp fibers by atomic force microscopy. *Journal of materials science* **44** (14), 3770–3776.
- HUANG, W.-X. , SHIN, S. J. & SUNG, H. J. 2007 Simulation of flexible filaments in a uniform flow by the immersed boundary method. *Journal of computational physics* **226** (2), 2206–2228.
- JEFFERY, G. B. 1922 The motion of ellipsoidal particles immersed in a viscous fluid. *Proceedings of the Royal Society of London. Series A, Containing papers of a mathematical and physical character* **102** (715), 161–179.
- JOUNG, C. , PHAN-THIEN, N. & FAN, X. 2001 Direct simulation of flexible fibers. *Journal of non-newtonian fluid mechanics* **99** (1), 1–36.

- KESHTKAR, M. , HEUZEY, M. & CARREAU, P. 2009 Rheological behavior of fiber-filled model suspensions: Effect of fiber flexibility. *Journal of Rheology* **53** (3), 631–650.
- KHAN, M. , MORE, R. V. & ARDEKANI, A. M. 2022 A constitutive model for viscosity of dense fiber suspension. *arXiv preprint arXiv:2211.07134* .
- KITANO, T. & KATAOKA, T. 1981 The rheology of suspensions of vinylon fibers in polymer liquids. i. suspensions in silicone oil. *Rheologica Acta* **20** (4), 390–402.
- KROMKAMP, J. , VAN DEN ENDE, D. T. , KANDHAI, D. , VAN DER SMAN, R. G. & BOOM, R. M. 2005 Shear-induced self-diffusion and microstructure in non-brownian suspensions at non-zero reynolds numbers. *Journal of fluid mechanics* **529**, 253–278.
- LINDSTRÖM, S. B. & UESAKA, T. 2008 Simulation of semidilute suspensions of non-brownian fibers in shear flow. *The Journal of chemical physics* **128** (2), 024901.
- LOBRY, L. , LEMAIRE, E. , BLANC, F. , GALLIER, S. & PETERS, F. 2019 Shear thinning in non-brownian suspensions explained by variable friction between particles. *Journal of Fluid Mechanics* **860**, 682–710.
- LUNDELL, F. , SÖDERBERG, L. D. & ALFREDSSON, P. H. 2011 Fluid mechanics of papermaking. *Annual Review of Fluid Mechanics* **43**, 195–217.
- MARI, R. , SETO, R. , MORRIS, J. F. & DENN, M. M. 2014 Shear thickening, frictionless and frictional rheologies in non-brownian suspensions. *Journal of Rheology* **58** (6), 1693–1724.
- MARON, S. H. & PIERCE, P. E. 1956 Application of ree-eyring generalized flow theory to suspensions of spherical particles. *Journal of colloid science* **11** (1), 80–95.
- MEWIS, J. & METZNER, A. 1974 The rheological properties of suspensions of fibres in newtonian fluids subjected to extensional deformations. *Journal of Fluid Mechanics* **62** (3), 593–600.
- MORE, R. & ARDEKANI, A. 2020a A constitutive model for sheared dense suspensions of rough particles. *Journal of Rheology* **64** (5), 1107–1120.
- MORE, R. & ARDEKANI, A. 2020b Roughness induced shear thickening in frictional non-brownian suspensions: A numerical study. *Journal of Rheology* **64** (2), 283–297.
- MORE, R. V. & ARDEKANI, A. M. 2020c Effect of roughness on the rheology of concentrated non-brownian suspensions: A numerical study. *Journal of Rheology* **64** (1), 67–80.
- MORE, R. V. & ARDEKANI, A. M. 2020d A unifying mechanism to explain the rate dependent rheological behavior in non-brownian suspensions: One curve to unify them all. *arXiv preprint arXiv:2011.07038* .
- NAWAB, M. & MASON, S. 1958 Viscosity of dilute suspensions of thread-like particles. *The Journal of Physical Chemistry* **62** (10), 1248–1253.
- OKAGAWA, A. & MASON, S. 1973 The kinetics of flowing dispersions. vii. oscillatory behavior of rods and discs in shear flow. *Journal of Colloid and Interface Science* **45** (2), 330–358.
- PESKIN, C. S. 1972 Flow patterns around heart valves: a numerical method. *Journal of computational physics* **10** (2), 252–271.
- PETRICH, M. P. , KOCH, D. L. & COHEN, C. 2000 An experimental determination of the stress–microstructure relationship in semi-concentrated fiber suspensions. *Journal of non-newtonian fluid mechanics* **95** (2-3), 101–133.
- PINELLI, A. , OMIIDYEGANEH, M. , BRÜCKER, C. , REVELL, A. , SARKAR, A. & ALINOVI, E. 2017 The pelskin project: part iv—control of bluff body wakes using hairy filaments. *Meccanica* **52** (7), 1503–1514.
- ROMA, A. M. , PESKIN, C. S. & BERGER, M. J. 1999 An adaptive version of the immersed boundary method. *Journal of computational physics* **153** (2), 509–534.
- SALAHUDDIN, A. , WU, J. & AIDUN, C. 2012 Numerical study of rotational diffusion in sheared semidilute fibre suspension. *Journal of fluid mechanics* **692**, 153–182.
- SALAHUDDIN, A. , WU, J. & AIDUN, C. 2013 Study of semidilute fibre suspension rheology with lattice-boltzmann method. *Rheologica Acta* **52** (10-12), 891–902.
- SEGEL, L. A. & HANDELMAN, G. H. 2007 *Mathematics applied to continuum mechanics*. SIAM.
- SEPEHR, M. , CARREAU, P. J. , MOAN, M. & AUSIAS, G. 2004 Rheological properties of short fiber model suspensions. *Journal of Rheology* **48** (5), 1023–1048.
- SNOOK, B. , DAVIDSON, L. M. , BUTLER, J. E. , POULIQUEN, O. & GUAZZELLI, E. 2014 Normal stress differences in suspensions of rigid fibres. *Journal of fluid mechanics* **758**, 486.

- STICKEL, J. J. , KNUTSEN, J. S. , LIBERATORE, M. W. , LUU, W. , BOUSFIELD, D. W. , KLINGENBERG, D. J. , SCOTT, C. T. , ROOT, T. W. , EHRHARDT, M. R. & MONZ, T. O. 2009 Rheology measurements of a biomass slurry: an inter-laboratory study. *Rheologica Acta* **48** (9), 1005–1015.
- SWITZER, L. H. & KLINGENBERG, D. J. 2003 Rheology of sheared flexible fiber suspensions via fiber-level simulations. *Journal of Rheology* **47** (3), 759–778.
- TANNER, R. I. & DAI, S. 2016 Particle roughness and rheology in noncolloidal suspensions. *Journal of Rheology* **60** (4), 809–818.
- TAPIA, F. , SHAIKH, S. , BUTLER, J. E. , POULIQUEN, O. & GUAZZELLI, E. 2017 Rheology of concentrated suspensions of non-colloidal rigid fibres. *Journal of Fluid Mechanics* **827**.
- THALEN, N. 1964 Shear modulus and ultimate shear strength of some paper pulp fibre networks. *Svensk Papperstidn.* **67**, 259–264.
- TOWNS, J. , COCKERILL, T. , DAHAN, M. , FOSTER, I. , GAITHER, K. , GRIMSHAW, A. , HAZLEWOOD, V. , LATHROP, S. , LIFKA, D. , PETERSON, G. D. & OTHERS 2014 Xsede: accelerating scientific discovery. *Computing in science & engineering* **16** (5), 62–74.
- TOZZI, E. J. , KLINGENBERG, D. J. & SCOTT, C. T. 2008 Correlation of fiber shape measures with dilute suspension properties. *Nordic Pulp & Paper Research Journal* **23** (4), 369–373.
- WILLIAMS, S. R. & PHILIPSE, A. P. 2003 Random packings of spheres and spherocylinders simulated by mechanical contraction. *Phys. Rev. E* **67**, 051301.
- WU, J. & AIDUN, C. K. 2010a A method for direct simulation of flexible fiber suspensions using lattice boltzmann equation with external boundary force. *International Journal of Multiphase Flow* **36** (3), 202–209.
- WU, J. & AIDUN, C. K. 2010b A numerical study of the effect of fibre stiffness on the rheology of sheared flexible fibre suspensions. *Journal of fluid mechanics* **662**, 123–133.
- YAMAMOTO, S. & MATSUOKA, T. 1993 A method for dynamic simulation of rigid and flexible fibers in a flow field. *The Journal of chemical physics* **98** (1), 644–650.
- YAMANE, Y. , KANEDA, Y. & DIO, M. 1994 Numerical simulation of semi-dilute suspensions of rodlike particles in shear flow. *Journal of non-newtonian fluid mechanics* **54**, 405–421.